High magnetic field phase diagram and failure of the magnetic Grüneisen scaling in $LiFePO_4$

J. Werner,[1,*] S. Sauerland,[1] C. Koo,[1] C. Neef,[1] A. Pollithy,[1] Y. Skourski,[2] and R. Klingeler[1,3]

[1]*Kirchhoff Institute of Physics, Heidelberg University, INF 227, D-69120 Heidelberg, Germany*

[2]*Dresden High Magnetic Field Laboratory (HLD-EMFL), Helmholtz-Zentrum Dresden Rossendorf, D-01314 Dresden, Germany*

[3]*Centre for Advanced Materials (CAM), Heidelberg University, INF 225, D-69120 Heidelberg, Germany*

(Received 28 February 2019; revised manuscript received 8 May 2019; published 24 June 2019)

We report the magnetic phase diagram of single-crystalline $LiFePO_4$ in magnetic fields up to 58 T and present a detailed study of magnetoelastic coupling by means of high-resolution capacitance dilatometry. Large anomalies at T_N in the thermal-expansion coefficient α imply pronounced magnetoelastic coupling. Quantitative analysis yields the magnetic Grüneisen parameter $\gamma_{mag} = 6.7(5) \times 10^{-7}$ mol/J. The positive hydrostatic pressure dependence $dT_N/dp = 1.46(11)$ K/GPa is dominated by uniaxial effects along the a axis. Failure of Grüneisen scaling below $\approx$40 K, i.e., below the peak temperature in the magnetoelectric coupling coefficient [7], implies several competing degrees of freedom. A broad and strongly magnetic field dependent anomaly in α in this temperature regime highlights the relevance of structure changes. Upon application of the magnetic field $B||b$ axis, a pronounced jump in the magnetization implies spin reorientation at $B_{SF} = 32$ T as well as a precursing phase at 29 T and $T = 1.5$ K. In a two-sublattice mean-field model, the saturation field $B_{sat,b} = 64(2)$ T enables assessing the effective antiferromagnetic exchange interaction $J_{af} = 2.68(5)$ meV as well as anisotropies $D_b = -0.53(4)$ meV and $D_c = 0.44(8)$ meV.

DOI: 10.1103/PhysRevB.99.214432

I. INTRODUCTION

In addition to exceptionally high applicability of lithium orthophosphates [1–3] for electrochemical energy storage in Li-ion batteries, competing magnetic interactions, magnetic anisotropy, and coupling of spin and electric degrees of freedom yield complex magnetic behavior in $LiMPO_4$ (M = Mn, Fe, Co, Ni). The resulting rich physics is, e.g., demonstrated by ferrotoroidicity in $LiCoPO_4$ and $LiNiPO_4$ [4–6]. In general, depending on the actual transition metal, $LiMPO_4$ develops long-range antiferromagnetic order at low temperatures and exhibits a large magnetoelectric effect in the magnetically ordered phase [7–9]. The known magnetic phase diagrams of this family are rather complex, featuring incommensurate spin configurations, frustration, and usual magnetic excitations [8,10–15].

Magnetic phase diagrams have been reported for all lithium orthophosphates [13–15] except for $LiFePO_4$. At $B = 0$ T, $LiFePO_4$ develops long-range antiferromagnetic order of $S = 2$ spins of the magnetic Fe^{2+} ions below $T_N = 50$ K [16]. The ordered moment amounts to $4.09\mu_B$ [7,17] and the spins are mainly directed along the crystallographic b axis (space group *Pnma*) [17]. Besides, the ground state features a collinear rotation of the spins towards the a axis as well as spin canting along the c axis with an overall rotation of the ordered moments of $1.3(1)^\circ$ off the b axis [7,18]. The observed spin canting suggests the presence of Dzyaloshinsky-Moriya (DM) interactions which may account for magnetoelectric coupling in $LiFePO_4$. In particular, as spin canting is not compatible with *Pnma* symmetry, a lower crystal symmetry might appear below T_N [7,19]. Even in the absence of spin canting, an alternative mechanism to the ME effect may originate from orbital magnetic moments responding to polar distortions induced by an applied electric field [20]. Magnetic interactions have been studied by various groups using inelastic neutron scattering (INS) which implies competing antiferromagnetic interactions of however contradicting magnitude [7,18,19]. When the INS data are analyzed including single-ion anisotropy which is strongly suggested by the results presented at hand, the dominating magnetic exchange is found in the bc direction, i.e., $J_{bc} \approx 0.46$ and 0.77 meV, respectively, which is by a factor of 2–4 smaller than D [7,18]. In addition, rather dispersionless low-energy excitations have been found to persist up to 720 K which are discussed in terms of single-ion spin splitting [18].

Here we report the magnetic phase diagram and magnetoelastic coupling in $LiFePO_4$. Pronounced anomalies in the thermal-expansion coefficients as well as pulsed-field magnetization data are used to construct the magnetic phase diagram. The data imply spin reorientation at $B_{SF}\|b = 32$ T as well as a precursing phase at 29 T. B_{SF} and B_{sat} are discussed in a two-sublattice mean-field model which yields effective antiferromagnetic exchange interaction $J_{af} = 2.68(5)$ meV and anisotropies $D_b = -0.53(4)$ meV and $D_c = 0.44(8)$ meV. High-resolution dilatometry enables detailed studies of the interplay of spin, structure, and dielectric degrees of freedom. The magnetic Grüneisen parameter is determined as $\gamma_{mag} = 6.7(5) \times 10^{-7}$ mol/J for $T \geqslant 40$ K. At lower temperatures, failure of Grüneisen scaling indicates the presence of at least two competing degrees of freedom. Notably, a broad feature in the thermal-expansion coefficient in the same temperature range further demonstrates the intimate coupling of spin, charge, and structure in $LiFePO_4$.

*johannes.werner@kip.uni-heidelberg.de

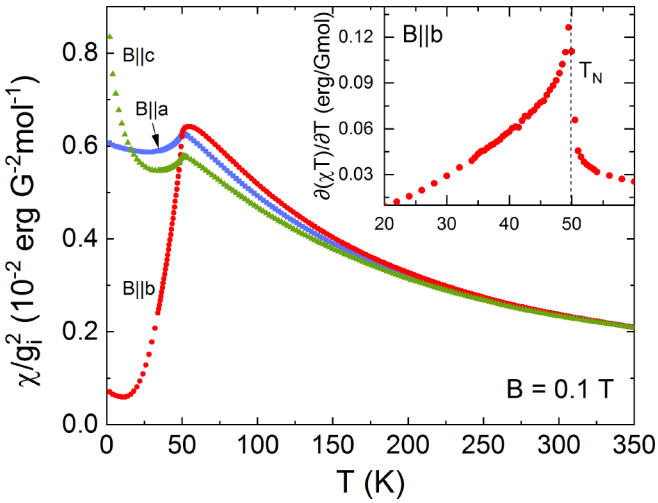

FIG. 1. Static magnetic susceptibility $\chi = M/B$ of $LiFePO_4$ vs temperature for $B = 0.1$ T applied along the three crystallographic axes. The data have been normalized by the respective components of the g tensor as fitted to the high-temperature behavior (see the text). Inset: Corresponding derivative $\partial(\chi T)/\partial T$.

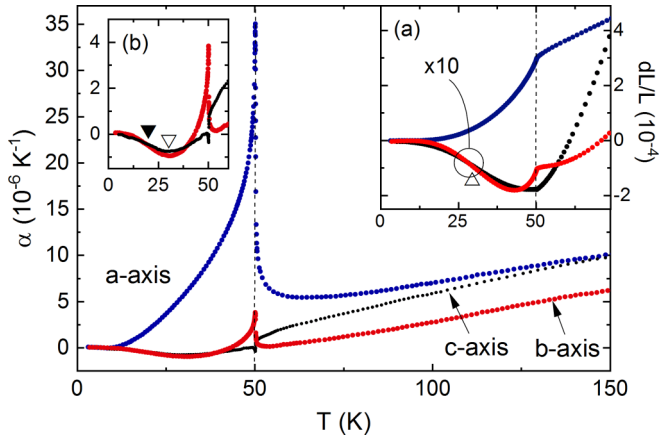

FIG. 2. Thermal-expansion coefficient α along the three crystallographic axes. The dashed line shows T_N. Insets: (a) Associated relative length changes dL/L. Data for the b and c axis have been multiplied by 10. (b) Thermal-expansion coefficient along the b and c axis up to 60 K. Open (filled) triangles label the temperatures T_m^* (T^*) of a minimum (increase) in α (see the text).

II. EXPERIMENT

Single crystals of $LiFePO_4$ were grown by the high-pressure optical floating-zone method as reported in detail in Ref. [21]. Magnetization in static magnetic fields up to 5 T was studied by means of a Quantum Design MPMS-XL5 superconducting quantum interference device magnetometer and in fields up to 15 T in a home-built vibrating sample magnetometer (VSM) [22]. Pulsed-magnetic-field magnetization was studied up to 58 T at Helmholtz Zentrum Dresden Rossendorf by the induction method using a coaxial pick-up coil system [23]. The pulse raising time was 7 ms. The pulsed-field magnetization data were calibrated using static magnetic field measurements. The relative length changes dL/L were studied on a cuboidal-shaped crystal with dimension of $3 \times 3 \times 2$ mm^3. The measurements were done by means of a three-terminal high-resolution capacitance dilatometer [24]. In order to investigate the effect of magnetic fields, the linear thermal-expansion coefficients $\alpha_i = 1/L_i \cdot dL_i(T)/dT$ have been studied in magnetic fields up to 15 T which were applied along the direction of the measured length changes $i = a, b, c$. In addition, the field-induced length changes were measured at various fixed temperatures in magnetic fields up to 15 T and the longitudinal magnetostriction coefficient $\lambda_i = 1/L_i \cdot dL_i(B_i)/dB_i$ was derived.

III. EXPERIMENTAL RESULTS

A. Static magnetic susceptibility

The onset of long-range antiferromagnetic order in $LiFePO_4$ at $T_N = 50.0(5)$ K is associated with pronounced anomalies in the magnetic susceptibility and in the thermal expansion (Figs. 1 and 2). The magnetic susceptibility implies that the crystallographic b axis is the easy magnetic axis which is in agreement with previous studies. [16,17] At high temperatures, the magnetic susceptibility obeys Curie-Weiss behavior and the differences in magnetization along the crystallographic axes can be associated to the anisotropy of the g tensor. The data have hence been corrected by respective values of the g factor g_i, which have been obtained by fitting the volume susceptibility by means of a Curie-Weiss law and obtaining the best overlap of χ_i at high temperatures. This procedure yields $g_a = 2.24(3)$, $g_b = 2.31(2)$, and $g_c = 1.99(3)$. Notably, below 250 K, the data imply anisotropy which is not associated with the g tensor as visualized by Fig. 1 [25]. We also mention a Curie-like upturn at low temperatures which is particularly pronounced for the $B \| c$ axis, thereby indicating the presence of anisotropic quasifree magnetic moments [cf. also Fig. 4(a)].

B. Thermal expansion

The evolution of long-range magnetic order at T_N is confirmed by sharp anomalies of the uniaxial thermal-expansion coefficients α_i ($i = a, b, c$) (Fig. 2). The λ-shaped anomalies confirm the continuous nature of the phase transition. The measured length changes dL/L shown in Fig. 2(a) signal shrinking of the a and b axes upon evolution of long-range magnetic order at T_N while there is a slight increase of the c axis. The anomalies confirm significant magnetoelastic coupling in $LiFePO_4$. The signs of the anomalies show positive uniaxial pressure dependence of T_N for pressure along the a and b axes, i.e., $\partial T_N/\partial p_i > 0$ for $i = a, b$, whereas there is only a tiny anomaly in α_c indicating $\partial T_N/\partial p_c$ being negative and small. T_N also shows significant positive hydrostatic pressure dependence as shown by a very large anomaly of the volume thermal-expansion coefficient (see the inset of Fig. 7).

Application of external magnetic fields yields suppression of the long-range antiferromagnetically ordered phase as visible by the effects of $B = 15$ T applied along the b and c axes, respectively, on the magnetic susceptibility shown in Fig. 4. Sharp anomalies of the thermal-expansion coefficients studied in various magnetic fields applied along the three crystallographic axes (Fig. 3) enable detailed determination of the phase boundaries. These measurements are backed up

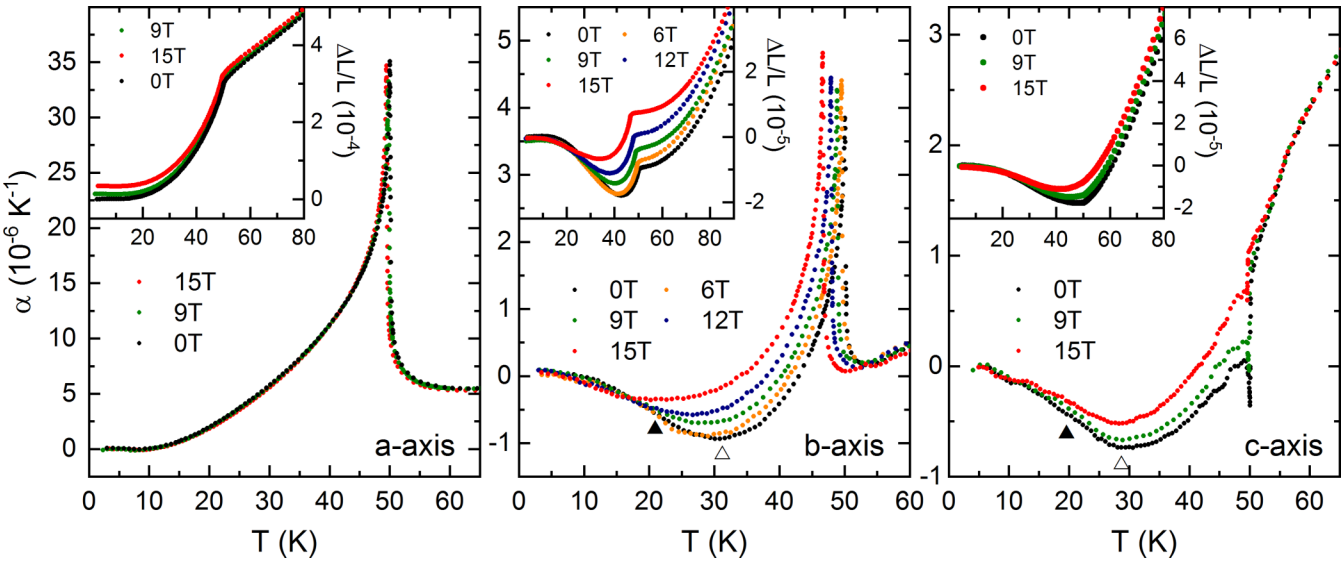

FIG. 3. Thermal-expansion coefficient α at magnetic fields between 0 and 15 T for all three crystallographic directions of $LiFePO_4$. Insets show the corresponding length change. Open (filled) triangles label the temperatures T_m^* (T^*) of a minimum (inflection point) in α (see the text).

by magnetostriction data at various temperatures (see Fig. S2 of the Supplemental Material [26]). While for the $B\|a$ axis neither T_N nor the shape of the anomaly in α_a are significantly affected by magnetic fields up to 15 T, the anomaly in α_c is reduced for $B\|c$ while T_N does not shift either. In contrast, for $B\|b$, T_N is clearly shifted at $B = 15\,T$ by $\Delta T_N \approx 3\,K$ [see Fig. 3(b)] while the shape of the anomalies in α_b is only very weakly affected. This observation corresponds to the effect of $B\|b = 15\,T$ on Fisher's specific heat [27] $\partial(\chi T)/\partial T$ presented in Fig. 4(b).

Moreover, at $B = 0\,T$, the thermal-expansion coefficients α_b and α_c exhibit an additional feature in the ordered phase, i.e., at $T < T_N$. As illustrated in Fig. 2(a), the length changes towards lowest temperatures undergo a minimum at approximately 43 K followed by a gradual increase to low temperatures. Correspondingly, there is a minimum (T_m^*, open triangles in Fig. 2) followed by a rise in α. Note that a similar feature may be present in α_a but might be masked by the large anomaly at T_N. Qualitatively, the data in Figs. 3(b) and 3(c) imply suppression of the associated phenomenon in applied magnetic fields as indicated by reduction of the characteristic temperatures T_m^* and T^* as well as of the size of the minimum and of the low-temperature hump. For a quantitative estimate of the field effect, in addition to the temperature of the minimum T_m^* we extract a characteristic temperature T^* at the inflection point of α_b which shifts from $T^*(0T) \approx 19\,K$ to about 11 K at $B\|b = 15\,T$.

C. Magnetization

The magnetization M vs B at $T = 1.5\,K$ along the three crystallographic axes is shown in Fig. 5. At $T = 1.5\,K$, there is a jumplike increase of $M(B\|b)$ suggesting spin reorientation at $B_{SF} = 32\,T$ in accord with the easy-axis inferred from Fig. 1. The anomaly amounts to $\Delta M = 1.39(3)\,\mu_B/f.u.$ Note that in the two-sublattice model presented below, ΔM corresponds to a change of the angle between the spins from antiparallel to about 145°. For $B > B_{SF}$ applied along b, M increases linearly similar to what is observed for $M(B \perp b)$. At $T = 1.5\,K$, none of the high-field magnetization curves show signatures of saturation up to 58 T. At small magnetic fields, there is right bending of the magnetization curves which implies the presence of quasifree spins. Notably, this behavior significantly depends on the magnetic field direction. It is most pronounced for $B\|c$ in agreement to the Curie-like contribution to $\chi(T)$ which is largest for this field direction (cf. Fig. 1). Quantitatively, fitting the magnetization curves by a Brillouin function $B_{1/2}$ plus a linear term describes the data for $B \perp c$ very well. The data indicate $M_{qf\perp c} \approx 0.08\,\mu_B/f.u.$ for the response associated with quasifree (qf) spins, Whereas the curvature seen in M vs $B||c$ suggests much larger moments or a strongly anisotropic g factor. The behavior in M vs $B||c$ agrees with the effect on χ vs T. As shown in Fig. 4(a), the Curie-like upturn at $T < 10\,K$ is most pronounced for $B||c$ but completely suppressed at $B = 15\,T$.

The rather linear behavior of M for $B > B_{SF}$ applied along b does not extrapolate to the origin of the graph. Hence, while the transition may be attributed to spin reorientation,

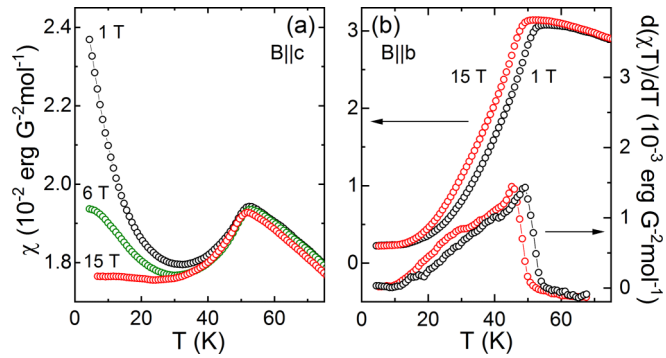

FIG. 4. Static magnetic susceptibility χ at $T < 80\,K$ for (a) $B||c$ axis at 1, 6, and 15 T. (b) χ and $\partial(\chi T)/\partial T$ for $B||b$.

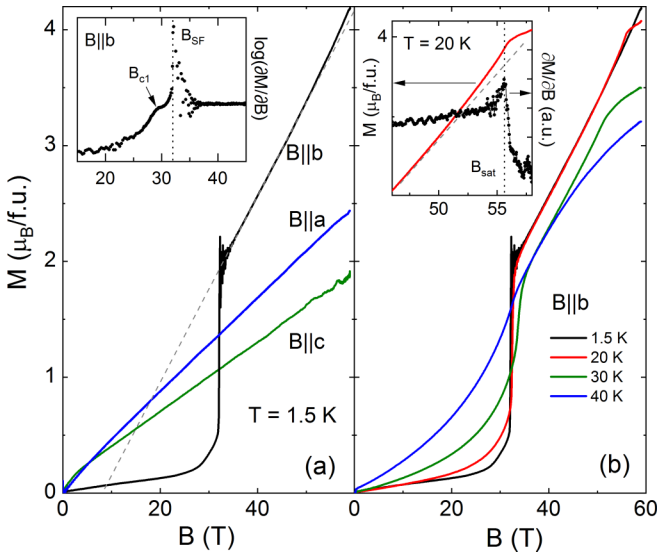

FIG. 5. (a) Pulsed-field magnetization for all three crystallographic directions of $LiFePO_4$, at 1.5 K, and (b) for $B||b$ axis at various temperatures $1.5 \leqslant T \leqslant 40$ K. All data have been obtained upon downsweep of B. Insets: (a) Magnetic susceptibility, at 1.5 K, for $B||b$ (logarithmic scale) highlighting spin reorientation as well as an anomaly at B_{C1}. (b) Magnetization and magnetic susceptibility in the vicinity of the saturation field B_{sat}. The (grey) dashed lines show linear extrapolation of the data.

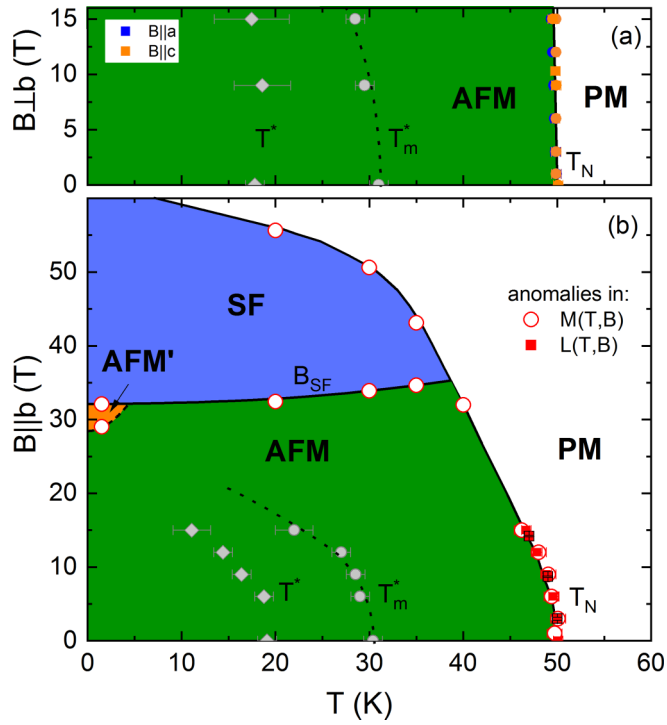

FIG. 6. Magnetic phase diagram of $LiFePO_4$ for (a) $B||a$ (blue markers), $B||c$ (orange) and (b) $B||b$ (red) as constructed from thermal-expansion/magnetostriction (squares) and magnetization (circles) measurements. The lines are guides to the eye. AFM, AFM′, SF, and PM label antiferromagnetically ordered, spin-reoriented, and paramagnetic phases, respectively. T_N, B_{C1}, and B_{SF} label the associated anomaly temperatures and fields. T^* (T^*_m) labels the inflection point (minimum) associated with the low-temperature features in α_b and α_c (grey markers; see the text).

it is not associated with a simple spin-flop behavior. This is corroborated by a more detailed inspection of the anomaly as highlighted by the susceptibility $\partial M/\partial B$ in Fig. 5. In addition to the jump at B_{SF}, there is a precursing broad steplike increase of $\partial M/\partial B$ towards a small plateau. The small step extends from ∼26 to 29 T [the latter is labeled B_{C1} in the inset of Fig. 5(a)]. The entire nonlinear changes associated with B_{C1} and B_{SF} sum up to $\Delta M = 1.74(5)\ \mu_B$/f.u. While there is no visible hysteresis for either $B \perp b$ or $B > B_{SF}$ applied along b.

Upon heating, the anomaly at B_{C1} vanishes. The magnetization jump at B_{SF} decreases and is smeared out while the critical field changes only very weakly [Fig. 5(b)]. At the same time, at higher temperature the saturation field appears to be visible in the accessible field range. At $T = 20$ K, we find $B_{sat} = 56(3)$ T which is well identified by a peak in $\partial M/\partial B$ [see the inset of Fig. 5(b)]. In addition, there is slight left bending of M vs B just below B_{sat}. The almost straight shape of the M vs B curve, however, evidence the lack of spin fluctuations in the vicinity of the upper critical field which is in agreement with a predominant three-dimensional (3D) character of magnetism as concluded from the size of the ordered magnetic moment [7,28].

D. Magnetic phase diagram

The magnetic phase diagram shown in Fig. 6 summarizes the evolution of the anomalies observed in the thermal expansion, magnetostriction, and magnetization upon application of external magnetic fields. For $B \perp b$, the data display the anomaly at $T_N(B)$ which is only weakly field dependent. In particular, the phase boundaries $T_N(B)$ for fields parallel to the a and c axis overlap and magnetization, specific-heat, and thermal-expansion measurements show $\partial T_N/\partial B = 0.023(8)$ K/T.

For the $B||b$ axis, a much more pronounced field effect is observed. For small B, i.e., in the vicinity of T_N, $\partial T_N/\partial B = 0.083(4)$ K/T is reviled. Extrapolating the phase boundary $T_N(B)$ to low temperatures suggests $B_{sat}(B||b) = 64(2)$ T. In addition, at $B_{SF}(T = 1.5\ \text{K}) \approx 32.0(1)$ T, a spin-reoriented phase (SF) evolves. B_{SF} is almost temperature independent. A rough estimate by means of a Clausius-Clapeyron relation $\Delta S = -\Delta M \partial B/\partial T \approx 0.15$ J/(mol K) implies only insignificant entropy changes associated with this transition [29]. At $T = 1.5$ K, there is a precursing anomaly in $M(B)$ indicating the presence of a competing antiferromagnetic phase AFM′ evolving at $B_{C1} = 29$ T. Finally, the phase diagram in Fig. 6 presents characteristic temperatures/fields associated with the feature in the thermal-expansion coefficient discussed above which signals structure-dielectric coupling. Figure 6 displays the characteristic temperatures T^* and T^*_m of the inflection point and the minimum in α, respectively.

IV. DISCUSSION

Comparing the nonphononic contributions to the specific heat and to the thermal-expansion coefficient enables further conclusions on the nature of the associated ordering

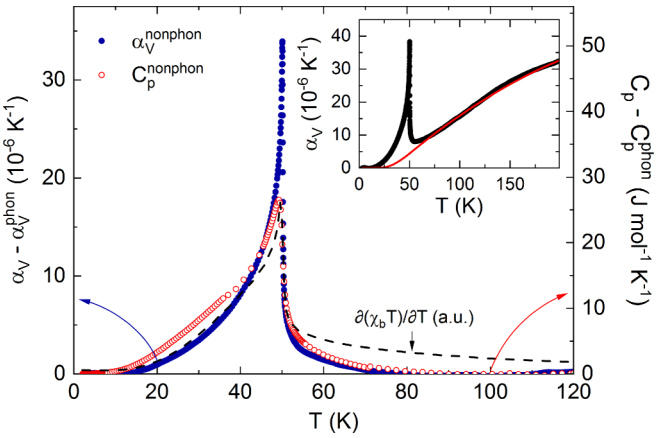

FIG. 7. Grüneisen scaling of the nonphononic contributions to the heat capacity (uncorrected c_p data have been taken from Ref. [30]) and volume thermal-expansion coefficient. The dashed line shows $\partial(\chi_b T)/\partial T$ (see the inset of Fig. 1). The inset shows the volume thermal-expansion coefficient α_v (black markers) with a combined Debye-Einstein fit at high temperatures (red line).

phenomena. In order to clarify the presence of one or more relevant energy scales, the volume thermal-expansion coefficient α_v (Fig. 7 inset) as derived by adding the uniaxial coefficients α_i is to be compared with the respective entropy changes as measured by the specific heat. For this comparison we use specific-heat data by Loos *et al.* [30] obtained on polycrstalline $LiFePO_4$. To be specific, for a comprehensive Grüneisen analysis, the lattice contributions of both α_v and c_p have to be separated. Extending the analysis of lattice contributions to c_p in Ref. [30], α_v and c_p are simultaneously fitted at temperatures well above the magnetic anomalies by means of a combined model consisting of a sum of Debye and Einstein terms:

$$c_p^{ph} = 3n_D R \times D(\Theta_D/T) + 3n_E R \times E(\Theta_E/T), \quad (1)$$

$$\alpha_V^{ph} = \gamma_D\, 3n_D R \times D(\Theta_D/T) + \gamma_E\, 3n_E R \times E(\Theta_E/T). \quad (2)$$

Debye D and Einstein function E depend on their characteristic temperatures Θ_D and Θ_E, respectively. While R denotes the universal gas constant, $3n_D$ and $3n_E$ account for the number of modes associated with each contribution so that their sum $n_D + n_E$ should yield the number of atoms in the unit cell. The use of two Grüneisen parameters γ_D and γ_E accounts for different Grüneisen scalings for the individual summands and is necessary as the contributions cannot be treated separately in the investigated temperature range. The fit for α_v is depicted together with the measured data in the inset of Fig. 7. The procedure yields a good description of the high-temperature behavior with $n_D = 3.77$ mol^{-1}, $n_E = 2.29$ mol^{-1}, $\Theta_D = 833$ K, $\Theta_E = 229$ K. These values are consistent with the previous analysis of the specific-heat data [30]. The Grüneisen parameters γ_D and γ_E are 3.81×10^{-7} and 3.06×10^{-7} mol/J. Due to the fact that the analysis at hand employs a concomitant fit of both the length and entropy changes, it may be valuable to report the resulting entropy changes $S_{mag} = 12.4$ J/(mol K) obtained by integrating the data by Loos *et al.* corrected by the here obtained phononic background. This value is larger than in Ref. [30] and closer to the theoretically expected value of 13.38 J mol^{-1} K^{-1}.

Comparison of the nonphononic parts of c_p and α_v, i.e., the respective differences of the measured data to the phononic fits, enables investigating the Grüneisen ratio of the associated length and entropy changes. Accordingly, the (magnetic) thermal-expansion coefficient and specific heat are shown in the main part of Fig. 7. First, the data imply that the above-mentioned procedure yields reliable results as there is a large temperature regime where c_p^{mag} and α_p^{mag} are proportional to each other. The experimental data and their analysis hence clearly show that the entropy and length changes in this temperature regime are driven by one degree of freedom. It is tempting to attribute this mainly to the spin degrees of freedom, i.e., the entropy changes are of magnetic nature which is supported by the fact that the extracted nonphononic entropy changes ΔS nearly agree to the expected spin entropy. To be specific, while there is no magnetic contribution to c_p and α_v above ~90 K, the two quantities match well down to about 40 K, except for a discrepancy at T_N where rounding of c_p likely originates from the polycrystal sample used in Ref. [30] as well as the limited temperature resolution of the utilized relaxation method. Scaling yields the Grüneisen parameter $\gamma_{mag} = 6.7(5) \times 10^{-7}$ mol/J. This value is associated with the pressure dependence of T_N being $dT_N/dp = \gamma_{mag} T_N V_m = 1.5(1)$ K/GPa which is deduced using the molar volume $V_m = 43.6$ cm^3 [21] by applying the Ehrenfest relation.

Notably, however, the scaled data show a significant deviation from each other well below T_N at temperatures between roughly 10 and 45 K, i.e., Grüneisen scaling by means of γ_{mag} is not valid in this temperature regime. In general, failure of Grüneisen scaling implies the presence of additional relevant degrees of freedom. Here, it provides thermodynamic evidence that several dominant degrees of freedom are concomitantly relevant in the ordered phase. Phenomenologically, failure of Grüneisen scaling can be associated with the low-temperature upturn in length changes of the b and c axis, respectively, upon reducing the temperature. It also agrees with the temperature regime below the peak of the magnetoelectric coupling coefficient α_{xy} [7]. Note that neither our single-crystal magnetization data (Fig. 1) nor neutron data in Refs. [7,17] indicate a symmetry-preserving spin reorientation at zero magnetic field upon cooling. One must conclude that the low-temperature feature observed in the thermal expansion must be ascribed to one or more additional degrees of freedom not corresponding to only magnetic entropy which drives antiferromagnetic order at T_N.

One may speculate about linking the observed failure of Grüneisen scaling to spectroscopic properties of $LiFePO_4$. Yiu *et al.* [18] have detected rather dispersionless hybrid excitations which are discussed in terms of electron states arising from the crystal-field splitting and spin-orbit coupling. Employing the parameters from Ref. [18] for a Schottky-like model would imply broad humps in the specific heat and the thermal-expansion coefficient which are centered around 32 K. Such hump would be supposed to exhibit a different Grüneisen parameter as compared to T_N so that one may speculate whether failure of Grüneisen scaling in $LiFePO_4$ can be associated with the reported hybrid excitations.

The measured spin-flop field, at 1.5 K, and the extrapolated saturation field $B_{\mathrm{sat}}(B||b) = 64(2)$ T allow us to determine the effective antiferromagnetic exchange interaction J_{AF} and the anisotropy difference D_{b} between the easy axis (b axis) and the intermediate axis (a axis) in a two-sublattice mean-field model. It is described by

$$\mathcal{H} = J_{\mathrm{AF}} S_i \cdot S_j + D_{\mathrm{b}}\left(S_i^{b^2} + S_j^{b^2}\right) + g\mu_{\mathrm{B}} B \cdot (S_i + S_j) \quad (3)$$

with the magnetic field $B||b$, $g_b = 2.31$, S^b the spin component in the b direction, and μ_{B} the Bohr magneton. J_{AF} is the effective exchange interaction between the sublattices i and j. Intersublattice exchange interactions are not considered for this analysis. The Hamiltonian Eq. (3) is minimized so that the experimentally observed values of B_{SF}, B_{sat}, and M_{sat} are reproduced. The model yields $J_{\mathrm{AF}} = 2.68(5)$ meV and $D_{\mathrm{b}} = -0.53(4)$ meV. The minus sign of D signals that, at $B = 0$ T, spins align along the b axis. Extending the Hamiltonian by an additional anisotropy in the c direction, i.e., D_{c} similar to D_{b}, enables us to account for the different susceptibilities $\partial M/\partial B$ measured along the a and c axis [see Fig. 5(a)]. Quantitatively, we obtain the plane-type anisotropy $D_{\mathrm{c}} = 0.44(8)$ meV.

Though the Hamiltonian [Eq. (3)] provides only a basic model for evaluating magnetism in $LiFePO_4$ which neither covers the two-step nature of spin reorientation (i.e., the presence of the intermediate phase AFM′) nor takes into account that $M(B > B_{\mathrm{SF}})$ does not resemble a simple spin-flop scenario, the obtained anisotropy of $D_{\mathrm{b}} = -0.53(4)$ meV is in good agreement with values obtained by inelastic neutron scattering (INS) where $-0.62(2)$ meV [19] and $-0.86(1)$ meV [18] have been reported [31]. Also the effective exchange interaction $J_{\mathrm{AF}} = 2.68(5)$ meV deduced from the macroscopic data at hand is in good agreement with $J_{\mathrm{AF}} = 4(J_{\mathrm{bc}} + J_{\mathrm{ab}}) = 3.64(2)$ meV [19] and 2.20(6) meV [18] from INS, whereas $D_{\mathrm{c}} = 0.44(8)$ meV does not agree with the INS results 0.94(4) meV [19] and 1.37(2) meV [18,32].

The low-temperature upturn of static susceptibility as well as the right bending of the magnetization curves below $B = 10$ T indicate the presence of anisotropic quasifree moments. It has been shown [21] for single crystals $LiMn_{1-x}Fe_xPO_4$ that the presence of such anisotropic moments evolves with increasing iron content x. One may speculate that Fe^{2+} antisite disorder [21,33], i.e., the fact that Fe^{2+} ions which possess similar ionic radii as Li^+ ions to some extent reside on Li positions, may account for the quasifree moments. For the crystal at hand, antisite disorder was estimated to about 2.3(2)% [21].

V. SUMMARY

The reported experimental studies of pulsed- and static-field magnetization, thermal expansion, and magnetostriction of single-crystalline $LiFePO_4$ enable constructing the magnetic phase diagram. In addition, high-resolution dilatometry is used for quantitative analysis of the pronounced magnetoelastic coupling in $LiFePO_4$. The macroscopic data imply antiferromagnetic correlations well above T_{N} up to about 250 K. This is corroborated by observation of magnetic contributions to the thermal expansion which obey Grüneisen scaling far above T_{N}. Notably, recently reported temperature dependence of the magnetoelectric coupling coefficient α_{xy} [7] is associated with failure of Grüneisen scaling. Our data hence provide direct thermodynamic experimental evidence for the essential role of structure changes for magnetoelectric coupling in $LiFePO_4$. Upon application of magnetic fields, associated features are suppressed. In addition, for the $B||b$ axis and $T = 1.5$ K, a pronounced jump in the magnetization implies spin reorientation at $B_{\mathrm{SF}} = 32$ T as well as a precursing competing phase at 29 T. In a two-sublattice mean-field model, the saturation field $B_{\mathrm{sat,b}} = 64(2)$ T and the spin-flop field $B_{\mathrm{SF}} = 32.0(1)$ enable assessing the effective antiferromagnetic exchange interaction $J_{\mathrm{af}} = 2.68(5)$ meV as well as anisotropies $D_{\mathrm{b}} = -0.53(4)$ meV and $D_{\mathrm{c}} = 0.44(8)$ meV.

ACKNOWLEDGMENTS

The project was supported by Deutsche Forschungsgemeinschaft (DFG) through Grant No. KL 1824/13-1. We acknowledge the support of the HLD at HZDR, member of the European Magnetic Field Laboratory (EMFL). J.W. acknowledges support by the HGSFP and IMPRS-QD. S.S. acknowledges support by DFG through Grant No. KL 1824/6. Support by A. Wolter and S. Gaß (IFW Dresden) is appreciated. Discussions with M. Abdel-Hafez in the frame of the German-Egypt Research Fund (BMBF Project No. 01DH17036 FLIB) are acknowledged.

J.W. and S.S. contributed equally to this work.

[1] A. K. Padhi, K. S. Nanjundaswamy, and J. B. Goodenough, J. Electrochem. Soc. **144**, 1188 (1997).

[2] S.-Y. Chung, J. T. Bloking, and Y.-M. Chiang, *Materials For Sustainable Energy: A Collection of Peer-Reviewed Research and Review Articles from Nature Publishing Group* (World Scientific, Singapore, 2011), pp. 205–210.

[3] M. Park, X. Zhang, M. Chung, G. B. Less, and A. M. Sastry, J. Power Sources **195**, 7904 (2010).

[4] B. B. Van Aken, J.-P. Rivera, H. Schmid, and M. Fiebig, Nature (London) **449**, 702 (2007).

[5] B. B. Van Aken, J.-P. Rivera, H. Schmid, and M. Fiebig, Phys. Rev. Lett. **101**, 157202 (2008).

[6] A. S. Zimmermann, B. B. Van Aken, H. Schmid, J.-P. Rivera, J. Li, D. Vaknin, and M. Fiebig, Eur. Phys. J. B **71**, 355 (2009).

[7] R. Toft-Petersen, M. Reehuis, T. B. S. Jensen, N. H. Andersen, J. Li, M. D. Le, M. Laver, C. Niedermayer, B. Klemke, K. Lefmann, and D. Vaknin, Phys. Rev. B **92**, 024404 (2015).

[8] D. Vaknin, J. L. Zarestky, J.-P. Rivera, and H. Schmid, Phys. Rev. Lett. **92**, 207201 (2004).

[9] J.-P. Rivera, Ferroelectrics **161**, 147 (1994).

[10] T. B. S. Jensen, N. B. Christensen, M. Kenzelmann, H. M. Rønnow, C. Niedermayer, N. H. Andersen, K. Lefmann, M. Jiménez-Ruiz, F. Demmel, J. Li *et al.*, Phys. Rev. B **79**, 092413 (2009).

[11] S.-H. Baek, R. Klingeler, C. Neef, C. Koo, B. Büchner, and H.-J. Grafe, Phys. Rev. B **89**, 134424 (2014).

[12] C. Rudisch, H.-J. Grafe, J. Geck, S. Partzsch, M. v. Zimmermann, N. Wizent, R. Klingeler, and B. Büchner, Phys. Rev. B **88**, 054303 (2013).

[13] E. Fogh, R. Toft-Petersen, E. Ressouche, C. Niedermayer, S. L. Holm, M. Bartkowiak, O. Prokhnenko, S. Sloth, F. W. Isaksen, D. Vaknin *et al.*, Phys. Rev. B **96**, 104420 (2017).
[14] R. Toft-Petersen, N. H. Andersen, H. Li, J. Li, W. Tian, S. L. Bud'ko, T. B. S. Jensen, C. Niedermayer, M. Laver, O. Zaharko *et al.*, Phys. Rev. B **85**, 224415 (2012).
[15] R. Toft-Petersen, J. Jensen, T. B. S. Jensen, N. H. Andersen, N. B. Christensen, C. Niedermayer, M. Kenzelmann, M. Skoulatos, M. D. Le, K. Lefmann *et al.*, Phys. Rev. B **84**, 054408 (2011).
[16] R. Santoro and R. Newnham, Acta Crystallogr. **22**, 344 (1967).
[17] G. Rousse, J. Rodriguez-Carvajal, S. Patoux, and C. Masquelier, Chem. Mater. **15**, 4082 (2003).
[18] Y. Yiu, M. D. Le, R. Toft-Petersen, G. Ehlers, R. J. McQueeney, and D. Vaknin, Phys. Rev. B **95**, 104409 (2017).
[19] J. Li, V. O. Garlea, J. L. Zarestky, and D. Vaknin, Phys. Rev. B **73**, 024410 (2006).
[20] A. Scaramucci, E. Bousquet, M. Fechner, M. Mostovoy, and N. A. Spaldin, Phys. Rev. Lett. **109**, 197203 (2012).
[21] C. Neef, H. Wadepohl, H.-P. Meyer, and R. Klingeler, J. Cryst. Growth **462**, 50 (2017).
[22] R. Klingeler, B. Büchner, K.-Y. Choi, V. Kataev, U. Ammerahl, A. Revcolevschi, and J. Schnack, Phys. Rev. B **73**, 014426 (2006).
[23] Y. Skourski, M. D. Kuz'min, K. P. Skokov, A. V. Andreev, and J. Wosnitza, Phys. Rev. B **83**, 214420 (2011).
[24] J. Werner, W. Hergett, M. Gertig, J. Park, C. Koo, and R. Klingeler, Phys. Rev. B **95**, 214414 (2017).
[25] Correlation effects may extend to even higher temperatures which would affect the obtained g values. Independent on that, magnetic anisotropy beyond the g tensor extends to at least 250 K.
[26] See Supplemental Material at http://link.aps.org/supplemental/10.1103/PhysRevB.99.214432 for magnetostriction and additional static susceptibility measurements
[27] M. E. Fisher, Philos. Mag. **7**, 1731 (1962).
[28] S. Nishimoto, S.-L. Drechsler, R. O. Kuzian, J. van den Brink, J. Richter, W. E. A. Lorenz, Y. Skourski, R. Klingeler, and B. Büchner, Phys. Rev. Lett. **107**, 097201 (2011).
[29] U. Stockert, N. Leps, L. Wang, G. Behr, S. Wurmehl, B. Büchner, and R. Klingeler, Phys. Rev. B **86**, 144407 (2012).
[30] S. Loos, D. Gruner, M. Abdel-Hafiez, J. Seidel, R. Hüttl, A. U. Wolter, K. Bohmhammel, and F. Mertens, J. Chem. Thermodyn. **85**, 77 (2015).
[31] In Refs. [18,19] the anisotropy tensor was chosen such that $D_b = 0$, whereas the present work uses a notation with $D_a = 0$. Therefore, cited values have been converted into the notation of the present work.
[32] Note that the actual numbers depend on the g factors used in the analyses. In the present work, g values from high-temperature Curie-Weiss fitting have been used while the INS models employ $g = 2$.
[33] G. R. Gardiner and M. S. Islam, Chem. Mater. **22**, 1242 (2009).